

On the dynamics of magnetically driven elastic filaments

By MARCUS ROPER¹, RÉMI DREYFUS², JEAN BAUDRY²,
M. FERMIGIER³, J. BIBETTE² AND H. A. STONE¹

¹Division of Engineering and Applied Sciences, Harvard University, Cambridge, MA 02138, USA

²Laboratoire Colloïdes et Matériaux Divisés, ESPCI, 75005 Paris, France

³Laboratoire Physique et Mécanique des Milieux Hétérogènes, ESPCI, 75005 Paris, France

(Received 6 April 2005 and in revised form 30 December 2005)

Following a novel realization of low-Reynolds-number swimming (Dreyfus *et al.*, *Nature*, vol. 436, 2005, p. 862), in which self-assembled filaments of paramagnetic micron-sized beads are tethered to red blood cells and then induced to swim under crossed uniform and oscillating magnetic fields, the dynamics of magnetoelastic filaments is studied. The filament is modelled as a slender elastica driven by a magnetic body torque. The model is applied to experiments of Goubault *et al.* (*Phys. Rev. Lett.*, vol. 91, 2003, art. 260802) to predict the lifetimes of metastable static filament conformations that are known to form under uniform fields. A second experimental swimming scenario, complementary to that of Dreyfus *et al.* (2005), is described: filaments are capable of swimming even if not tethered to red blood cells. Yet, if both ends of the filament are left free and the material and magnetic parameters are uniform along its length then application of an oscillating transverse field can only generate homogeneous torques, and net translation is prohibited by symmetry. It is shown that fore–aft symmetry is broken when variation of the bending stiffness along the filament is accounted for by including elastic defects, which produces results consistent with the swimming phenomenology.

1. Introduction

Swimming at low Reynolds numbers has been studied extensively and it has long been appreciated that the reversibility of fluid flows in this regime prohibits net translation of any swimmer that utilizes a time-reversible stroke sequence. The simplest swimmer to break out of the reversibility trap is the three-link swimmer, proposed by Purcell (1977), yet only recently (Becker, Koehler & Stone 2003) has the direction that the swimmer would take been determined. Many ingenious swimmers have been proposed since. For example, Najafi & Golestanian (2004) have studied a linkage of three colinear spheres connected by a pair of rods of controllable lengths, while Avron, Kenneth & Oaknin (2005) demonstrated that two spheres connected by a single variable-length rod suffice, provided that volume transfer is permitted between the spheres.

Inspired by copious biological examples such as the common bacteria *E-Coli*, which swim by rotating rigid helicoidal flagella, or spermatozoa which pass bending waves from head to tail along their flexible flagella (Brennen & Winet 1977), theoretical attention has recently been focused upon ‘one-armed swimmers’ (Wiggins & Goldstein 1998; Camalet, Jülicher & Prost 1999; Lagomarsino, Capuani & Lowe 2003) – long

elastic filaments, which deform under the effect of localized or distributed torques. While hitherto modelling has needed to be confined either to micro-organisms or to simple experiments in which biological elements are directly manipulated in optical or magnetic traps (Wiggins *et al.* 1998), recent advances in micromechanical engineering now permit the creation of independently swimming filaments, and direct control over geometry – length and aspect ratio – material properties, torque generation, and the shape and size of the cargo linked to the driven filament (Dreyfus *et al.* 2005). It is now useful to ask fluid dynamical questions about the effects of varying these parameters upon the pattern of the stroke and effectiveness of swimming.

We focus on one realization of such a micromanipulable object. Under an applied uniform magnetic field superparamagnetic beads spontaneously and reversibly self-assemble into long filaments. Goubault *et al.* (2003) made filaments that could survive the removal of the magnetic field by adding polyacrylic acid during the assembly phase. This chemical is adsorbed to the surface of the beads and a permanent polymer bridge forms between any two beads brought into contact. The possible static conformations of such a chain under applied uniform magnetic fields were explored, and extremely long-lived hairpin and S-shaped structures discovered (Goubault *et al.* 2003). It was shown that the bending stiffness of the filament can be inferred from the conformation that it adopts under the static field. A similar method for permanently linking the beads in the filament was developed in Koenig *et al.* (2005): the particles are coated in streptavidin and short lengths (~ 100 nm) of biotin-tipped doubled-stranded DNA are added during assembly. Biotin binds strongly and specifically to the coating on the particles. In Dreyfus *et al.* (2005) the effects of dynamically evolving magnetic fields upon the chain shapes were studied and it was demonstrated that if a filament is given time to align with a uniform magnetic field, and then a transverse-oscillating field applied, the chain may begin to swim in the direction of the uniform field. An additional condition must be met, which we shall show to proceed from the requirement that fore–aft symmetry be broken, and can be satisfied if for instance one end of the filament is tethered to a high-drag body such as red blood cell. Cēbers (2005) has analysed numerically a related scenario from the same class of experiments: the hairpin configurations are also capable of swimming under transverse-oscillating fields (Dreyfus 2005).

Slender-body theory will be used to model the drag on a magnetically actuated swimmer. In §2 the equations of motion for an elastica subject to magnetic torques are derived. As a test of this treatment of the dynamics in §3 we present a combined analytical and numerical analysis of the onset of instability in a filament initially orthogonal to the external field and of the stability of a hairpin. With this analysis we seek to determine bounds on the number of stable loops that can be formed in a filament as a function of the filament length and field strength. In §4 we propose a swimming scenario in which fore–aft symmetry is broken by elastic defects naturally present in the filament.

2. Developing equations of motion

In typical experiments the paramagnetic particles are spherical, with radii $a = 500$ nm, and chains consist of between thirty and a hundred particles yoked together (Dreyfus *et al.* 2005). We write $2L$ for the length of the filament. The particles are superparamagnetic, so when subjected to an applied field \mathbf{B} an otherwise isolated particle acquires a magnetic dipole moment $\mathbf{m} = (4\pi a^3/3\mu_0)\chi \cdot \mathbf{B}$, where $\mu_0 \equiv 4\pi \times 10^{-7}$ H m⁻¹ is the permeability of free space, and for complete generality

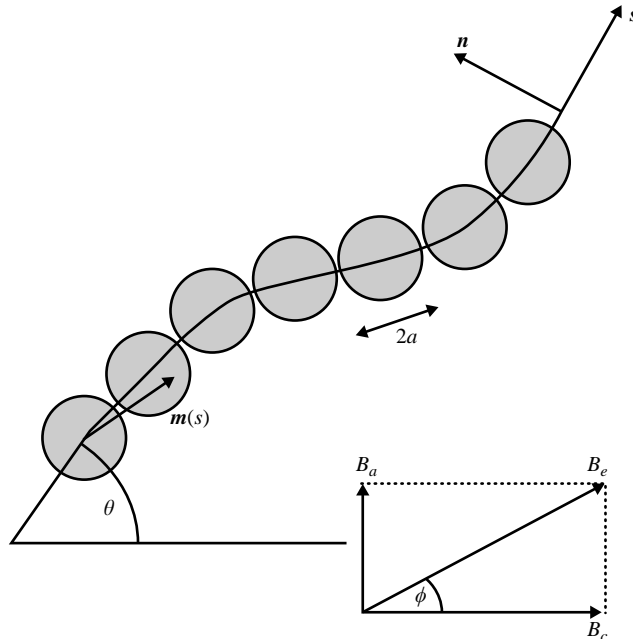


FIGURE 1. Schematic of paramagnetic filament, showing the conformation (θ) and field (ϕ) angles, and tangent (s) and normal (n) vectors.

we allow the *susceptibility* χ to have a tensorial character. Owing to slight anisotropies in the distribution of ferrite particles within the sphere the dipole moment upon the particle may not always align with the applied field, which means that a single particle may experience a magnetic torque under an external uniform field. This effect has been harnessed in the design of magnetic tweezers (Strick *et al.* 1996).

Define coordinate axes, so that the motion of the filament is confined to the (x, y) -plane, with the uniform field aligned with the x -axis, and the transverse field with the y -axis. We suppose a sinusoidally varying transverse field, and, referring to figure 1, decompose the total external field into components: $\mathbf{B}_e \equiv (B_c, B_a \equiv B_0 \sin \omega t, 0)$; the angle between the total field and the x -axis is denoted by $\phi(t)$. In experiments, the frequency, $f = \omega/2\pi$, of the transverse field can range from 0.1 up to 50 Hz. We will model the chain of particles as an elastica, with equivalent effective elastic and magnetic properties.

Denote by θ the angle that the filament centreline makes with the x -axis, and use the arclength $-L < s < L$ to parameterize along the centreline: the function $\theta(s, t)$ therefore encodes all information about the conformation of the elastica, and one pair of body-fixed coordinates (typically those of one of the free ends \mathbf{X} or of its centre of mass \mathbf{X}_{COM}) is then sufficient to describe fully the location of every material point. Additionally, it is convenient to decompose the velocity of the centreline into components $\mathbf{v} = v_s \mathbf{s} + v_n \mathbf{n}$ where we have introduced local tangent, normal and binormal vectors:

$$\mathbf{s} = (\cos \theta, \sin \theta, 0), \quad \mathbf{n} = (-\sin \theta, \cos \theta, 0), \quad \mathbf{b} = (0, 0, 1). \quad (2.1)$$

2.1. A model for the internal magnetic torque

Since both components of the external field are spatially homogenous, no net force is exerted on the swimmer. Instead internal torques are generated along the length

of the filament, in response to which the filament bends elastically. Previous models of one-armed swimmers have posited a simple sinusoidally varying internal torque, and with a few exceptions, such as Lagomarsino *et al.* (2003), linearize for long-wavelength deformations of the filament. Neither approximation is acceptable here, where we shall show that the torque depends in a nonlinear way on the conformation angle and does not inherit the simple sinusoidal time variation of the applied field, and where the angular deflection of the filament can easily become large. However, it is vital to our coarse-grained treatment of the elastic properties and to use of the slender-body approximation for the drag on the filament, that the radius of curvature (R) be much larger than the particle radius (a). Under the assumption that $a/R \ll 1$ one can account systematically for the magnetic interactions between particles at different orders of separation along the filament.

During filament self-assembly, we expect the particles to align with their directions of maximum susceptibility along the filament axis. To account for anisotropy of particle magnetizability, define two principal susceptibilities: one for the tangential direction (χ_{\parallel}) and one for the normal (χ_{\perp}) so that $\boldsymbol{\chi} = \chi_{\parallel}\mathbf{s}\mathbf{s} + \chi_{\perp}(\mathbf{1} - \mathbf{s}\mathbf{s})$. We also consider the effect of dipole–dipole interactions between the particles. A single particle in the chain having some dipole moment $\mathbf{m} \equiv m_s\mathbf{s} + m_n\mathbf{n}$ will create a field that is felt by all of the other particles in the chain, and at a point distance r away in the direction \mathbf{s} is given by $\mathbf{B}_{dip} = \mu_0(2m_s\mathbf{s} - m_n\mathbf{n})/4\pi r^3$. Because the dipole field decays very rapidly, we regard each bead as feeling only the external field and that of its nearest two neighbours and so neglect interactions between next-nearest neighbours and other more distant particles. Moreover, if we write R for the radius of curvature of the filament centreline, then up to some $O(a^2/R^2)$ correction the dipole moments of any triplet of nearest neighbours will be identical. The common dipole moment \mathbf{m} is then given implicitly by the equation

$$\mu_0\mathbf{m} = \frac{4}{3}\pi a^3 \boldsymbol{\chi} \cdot \left(\mathbf{B}_e + \mu_0 \frac{2m_s\mathbf{s} - m_n\mathbf{n}}{16\pi a^3} \right), \quad (2.2)$$

which can be solved for the tangential and normal components of the magnetization moment:

$$m_s = \frac{\frac{4}{3}\pi a^3 \chi_{\parallel} B_s}{\mu_0(1 - \chi_{\parallel}/6)}, \quad m_n = \frac{\frac{4}{3}\pi a^3 \chi_{\perp} B_n}{\mu_0(1 + \chi_{\perp}/12)}, \quad (2.3)$$

in which we have also decomposed the external field \mathbf{B}_e into normal and tangential components, respectively, $B_n = B_e \sin(\phi - \theta)$, $B_s = B_e \cos(\phi - \theta)$, with the orientational angles ϕ and θ being indicated in figure 1. The torque resultant per unit length of filament is then given by

$$\begin{aligned} \boldsymbol{\tau} &= \frac{1}{2a} \mathbf{m} \times \mathbf{B}_e = \frac{\pi a^2 B_e^2}{3\mu_0} \left(\frac{\chi_{\parallel} - \chi_{\perp} + \chi_{\parallel}\chi_{\perp}/4}{(1 - \chi_{\parallel}/6)(1 + \chi_{\perp}/12)} \right) \sin(2(\phi - \theta)) \mathbf{b} \\ &= \frac{2\pi a^2 B_c^2}{3\mu_0} \left(\frac{\chi_{\parallel} - \chi_{\perp} + \chi_{\parallel}\chi_{\perp}/4}{(1 - \chi_{\parallel}/6)(1 + \chi_{\perp}/12)} \right) S(\theta, t; b_0) \mathbf{b}, \end{aligned} \quad (2.4)$$

where we have trammelled all of the time and conformation dependence of the torque into a single dimensionless function:

$$S(\theta, t; b_0) \equiv b_0 \sin \omega t \cos 2\theta - \frac{1}{2}(1 - b_0^2 \sin^2 \omega t) \sin 2\theta. \quad (2.5)$$

Here $b_0 \equiv B_0/B_c$ is the dimensionless amplitude of the transverse field. Notice that both types of anisotropy, that inherent in the particles and that due to dipole–dipole interactions (which give the filament a larger susceptibility in the chain-tangential

direction than in the chain-normal direction), give rise to magnetic torques with the same angular dependence. We assume when making quantitative comparisons with experiment that dipole–dipole interactions are a much larger source of anisotropy, and so take $\chi_{\parallel} = \chi_{\perp} \equiv \chi$.

We can also estimate the error associated with the neglect of the next-nearest neighbour interactions. Suppose that the filament were straight so that (neglecting end effects) all the dipoles along its length were parallel. Then, a simple extension of the above derivation gives a similar expression for the components of the dipole moment, with χ replaced wherever it appears in the denominator by $\zeta(3)\chi$, where the Riemann-zeta prefactor is $\zeta(3) \approx 1.20$ (Zhang & Widom 1995; Martin & Andersen 1996). The sensitivity to conformation is similarly demonstrably small: with no impairment to the order of accuracy of our calculation, which is dominated by the errors in the hydrodynamic model, we may neglect such corrections.

2.2. The elastica with magnetic torques

For the experiments of Dreyfus *et al.* (2005) we may calculate a Reynolds number for the transverse motion of the filament $Re = \omega a^2/\nu \approx 10^{-5}$. The extreme smallness of this number implies that the inertia of the surrounding fluid may be neglected, and the only reaction force that it can exert against the motion of the filament is a Stokes drag. We can approximate for this using slender-body theory (Batchelor 1970). While the beads are not neutrally buoyant, their density does not greatly exceed that of the surrounding fluid, so that the inertia of the filament is similarly negligible.

The equations of motion for the filament follow from a balance between elastomagnetic and viscous stresses on an infinitesimal element of chain. We write Λ , N for the $s = \text{constant}$ cross-section-integrated tangential (tension) and normal stress resultants, $\mathbf{N} \equiv \Lambda \mathbf{s} + N \mathbf{n}$, and v_s and v_n for the corresponding local velocities of the filament, so that a force balance gives

$$\frac{\partial}{\partial s}(N \mathbf{n} + \Lambda \mathbf{s}) = \zeta(v_s \mathbf{s} + \alpha v_n \mathbf{n}). \quad (2.6)$$

Here ζ is the drag coefficient per unit length on the chain for motion parallel to the centreline, and α a drag anisotropy factor, which is equal to the ratio of drag coefficients for motion perpendicular to and parallel to the centreline of the body. For a chain far from any solid boundaries slender-body theory predicts $\zeta = 2\pi\eta/\log(2L/a)$ (where η is the viscosity of the fluid) and $\alpha = 2$ up to leading order in $\log(2L/a)$ (Batchelor 1970). For the present experiments we estimate $\log(2L/a) \approx 3$, and the error due to neglect of higher-order corrections to the drag constitutes the most severe defect of the model. In fact the filaments used in the experiments of Dreyfus *et al.* (2005) are denser than the surrounding fluid, and therefore sediment to the bottom of the capillary tube. The proximity of the wall leads to enormous enhancement of the wall drag, and this must be taken account of in order to achieve quantitative agreement with the experimental data.

The moment balance on an element of the elastica gives

$$\boldsymbol{\tau} + \frac{\partial \mathbf{M}}{\partial s} + \mathbf{s} \times \mathbf{N} = \mathbf{0}, \quad (2.7)$$

which relates the torque per unit length $\boldsymbol{\tau}$ which was derived in §2.1 to the cross-section integrated bending moment \mathbf{M} . The last term on the left-hand side represents a couple associated with the stresses acting across the ends of the element. We posit a simple constitutive relation $\mathbf{M} = K_b \kappa \mathbf{b}$, where $\kappa \equiv \partial\theta/\partial s$ is the curvature: The filament is assumed to be inextensible, with a uniform bending stiffness K_b . We expect this

coarse-graining of elastic properties to be acceptable provided that adjacent particles are not brought into contact, that is, the radius of curvature κ^{-1} is always much larger than a . Such a model was found to give good agreement on the static chain shapes, and it was shown that the filament bending stiffness K_b could be simply related to the stiffness (K_b^{link}) of the polymer bridges linking particles via a relation $K_b = 2aK_b^{link}/\ell$, where ℓ is the linker length (Goubault *et al.* 2003).

Next, recall the Serret–Frenet formulae

$$\frac{\partial \mathbf{s}}{\partial s} = \kappa \mathbf{n}, \quad \frac{\partial \mathbf{n}}{\partial s} = \kappa \mathbf{b} \times \mathbf{n} = -\kappa \mathbf{s}, \quad (2.8)$$

using which, the stress balance relation (2.6) can be separated into tangential and normal components:

$$\zeta v_s = \frac{\partial \Lambda}{\partial s} - \kappa N, \quad \alpha \zeta v_n = \frac{\partial N}{\partial s} + \kappa \Lambda. \quad (2.9a, b)$$

The torque balance relation (2.7) is simply

$$N = -\Gamma S - K_b \frac{\partial^2 \theta}{\partial s^2} \quad \text{with} \quad \Gamma \equiv \frac{2\pi a^2 B_c^2}{3\mu_0} \frac{\chi = -\chi_\perp + \chi_\parallel \chi_\perp / 4}{(1 - \chi_\parallel / 6)(1 + \chi_\perp / 12)}. \quad (2.10)$$

We use this result to substitute for N in the above. Now $\mathbf{s} \cdot \mathbf{s} = 1$ so that $\mathbf{s} \cdot d\mathbf{s}/dt = 0$, and consequently

$$\frac{d\mathbf{s}}{dt} = (\mathbf{s} \cdot \nabla) \mathbf{v} = \frac{d\mathbf{v}}{ds} = \left(\frac{\partial v_s}{\partial s} - \kappa v_n \right) \mathbf{s} + \left(\frac{\partial v_n}{\partial s} + \kappa v_s \right) \mathbf{n}. \quad (2.11)$$

Hence the inextensibility condition becomes $\partial v_s / \partial s = \kappa v_n$ or in terms of the system variables θ and Λ :

$$\alpha \frac{\partial^2 \Lambda}{\partial s^2} = \kappa^2 \Lambda - \left((\alpha + 1) \kappa \frac{\partial}{\partial s} + \alpha \frac{\partial \kappa}{\partial s} \right) \left(K_b \frac{\partial^2 \theta}{\partial s^2} + \Gamma S \right). \quad (2.12)$$

Additionally the first Serret–Frenet formula can be reworked as

$$\frac{d\mathbf{s}}{dt} = \frac{d\theta}{dt} \mathbf{n} = \left(\frac{\partial \theta}{\partial t} + \frac{\partial \theta}{\partial s} \frac{ds}{dt} \right) \mathbf{n}, \quad (2.13)$$

with the last summand vanishing by inextensibility. Substituting this back into the kinematical statement (2.11), we obtain an equation of motion for $\theta(s, t)$ and $\Lambda(s, t)$ in the form

$$\alpha \zeta \frac{\partial \theta}{\partial t} = \frac{\partial}{\partial s} (\kappa \Lambda) + \alpha \kappa \frac{\partial \Lambda}{\partial s} + \left(\alpha \kappa^2 - \frac{\partial^2}{\partial s^2} \right) \left(K_b \frac{\partial^2 \theta}{\partial s^2} + \Gamma S \right). \quad (2.14)$$

A similar equation has been derived by Cēbers & Javaitis (2004) under the hypothesis of isotropic viscous drag.

We non-dimensionalize the equations of motion (2.14) and of inextensibility (2.12) according to the following prescription. Define dimensionless system variables, $t = \tilde{t}/\omega$, $s = L\tilde{s}$, and non-dimensionalize all of the stress resultants by a characteristic hoop stress, $\Lambda = K_b \tilde{\Lambda}/L^2$, in terms of which the equations of motion become (we immediately discard the tildes on dimensionless quantities)

$$\alpha \frac{\partial^2 \Lambda}{\partial s^2} = \left(\frac{\partial \theta}{\partial s} \right)^2 \Lambda - \left((\alpha + 1) \frac{\partial \theta}{\partial s} \frac{\partial}{\partial s} + \alpha \frac{\partial^2 \theta}{\partial s^2} \right) \left(\frac{\partial^2 \theta}{\partial s^2} + M_n S(\theta, t; b_0) \right), \quad (2.15a)$$

$$\Omega \frac{\partial \theta}{\partial t} = \frac{\partial^2 \theta}{\partial s^2} \Lambda + (\alpha + 1) \frac{\partial \theta}{\partial s} \frac{\partial \Lambda}{\partial s} + \left(\alpha \left(\frac{\partial \theta}{\partial s} \right)^2 - \frac{\partial^2 \theta}{\partial s^2} \right) \left(\frac{\partial^2 \theta}{\partial s^2} + M_n S(\theta, t; b_0) \right). \quad (2.15b)$$

The relative strength of magnetic to elastic effects (the ‘floppiness’ of the filament) is encoded into a single dimensionless group, which we refer to as the *magnetoelastic* number

$$M_n \equiv \frac{2\pi(aB_c L)^2}{3\mu_0 K_b} \frac{\chi_{=} - \chi_{\perp} + \chi_{=} \chi_{\perp} / 4}{(1 - \chi_{=} / 6)(1 + \chi_{\perp} / 12)}. \quad (2.16)$$

The other dimensionless numbers required for a complete description of the physics are the ratio of viscous-relaxation to magnetic time scales $\Omega = \alpha \omega \zeta L^4 / K_b$, the ratio of drag coefficients α , and – through the dimensionless torque $S(\theta, t; b_0)$ – the ratio of transverse to uniform fields b_0 . Typical experiments have $14a < L < 40a$, $b_0 \approx 1$, $1 < M_n < 10$ and $1/10 < \Omega < 100$.

Equations (2.15) must be supplemented by a total of six boundary conditions. If both ends of the filament are free, these take the form of vanishing bending moment, and normal and tensile stress conditions:

$$\frac{\partial \theta}{\partial s} = 0, \quad \frac{\partial^2 \theta}{\partial s^2} + M_n S(\theta, t) = 0, \quad \Lambda = 0, \quad (2.17)$$

at $s = \pm 1$. We see immediately that if the filament is started from a symmetric initial configuration ($\theta(s, 0) = \theta(-s, 0)$), such as being aligned with the uniform field at $t = 0$, then this symmetry will be preserved by the motion. This means, in particular, that the filament cannot select a direction to swim in: nor, since the flow is inertialess and instantaneous, can it be expected that small asymmetries (such as infinitesimal perturbations to the initial filament shape due to thermal motions) will be amplified, and allow this symmetry to be broken, as has been shown the case in instances of lift-based propulsion (Vandenbergh, Zhang & Childress 2004).

Throughout this work we solve the pair of equations (2.15), subject to various combinations of boundary conditions, using a numerical scheme in which spatial derivatives are approximated by second-order finite differences (with the number of evaluation points N_p covering a range $60 < N_p < 201$). The stiffness of the equations means that an implicit scheme is required for the time evolution. We use a variable-order, variable-step-length scheme based on Gear’s method (the *MATLAB* routine `ode15s`).

3. Linear dynamics of static shapes under a uniform steady magnetic field

Notice that the torque $S(\theta, t)$ vanishes when $\theta = \phi$ or $\theta = \phi + \pi/2$, so that the filament is either locally aligned or orthogonal to the direction of the applied field. In the absence of an oscillating transverse field ($\phi \equiv 0$) there are, accordingly, two possible straight equilibrium shapes: $\theta \equiv 0$ and $\theta \equiv \pi/2$. Only the first of these is stable; a filament slightly perturbed from the second configuration will either rearrange into the first or into one of a class of numerous metastable and long-lived hairpin shapes. We explore this evolution numerically, mimicking the methodology of Goubault *et al.* (2003), in which filaments were allowed to align with a uniform field, and then a much stronger field, oriented at 90° to the first is switched on, and the folded filaments imaged. Images of a filament evolving to a simple hairpin are given as the first seven panes of figure 2, and should be compared with numerical simulations of the same event shown in figure 3(a). If, as in this case, the filament is too short, or the field too weak, then the hairpin destabilizes, and the filament unfolds

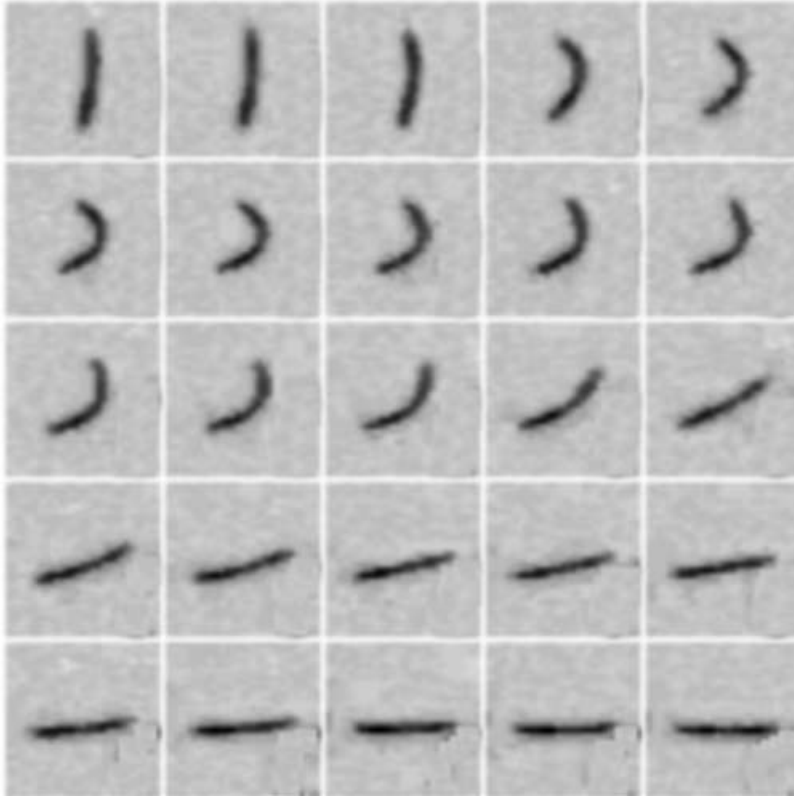


FIGURE 2. Evolution of a short filament to a hairpin, followed by unfolding and realignment. The filament is composed of a $13\ \mu\text{m}$ length of $750\ \text{nm}$ particles with measured bending stiffness $4.9 \times 10^{-24}\ \text{Jm}$, and field strength $B_c = 1.0\ \text{mT}$ corresponding to a magnetoelastic number of $M_n = 0.12$.

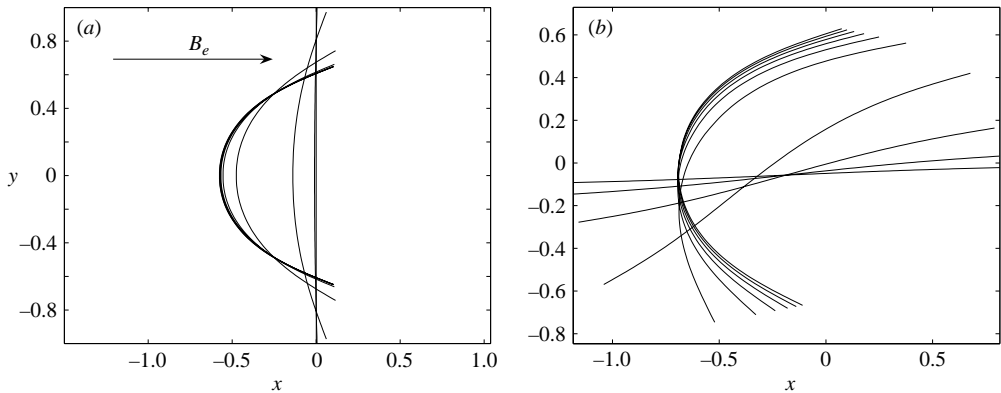


FIGURE 3. Prototypical evolution of a filament initially perpendicular to the applied magnetic field at moderate magnetoelastic number. (a) ($0 < t < 0.5$): odd-parity instability drives the filament away from the straightened state, and it evolves to metastable hairpin. (b) ($4.5 < t < 5.0$) the hairpin destabilizes; the filament relaxes to alignment with magnetic field. Here, $M_n = 6.0$ and the number of points in the spatial discretization is $N_p = 201$, with an initial perturbation of size $B_\beta = 10^{-3}$.

to come into complete alignment with the applied field, as shown in the remaining panes of figure 2 which should be compared with the numerical results presented in figure 3(b). The stability of the hairpin and S-shaped conformations is discussed in §3.2.

The complete classification of the metastable shapes is an unsolved matter. Here we take a first step toward providing such a classification by clarifying the dynamics of their formation – the growth of instability of the filament under a perpendicular applied field – and by presenting some numerical and asymptotic results on the lifetime of the simplest of the hairpin conformations. We argue that such stability considerations limit the number of folds that can be resolved in the experiments of Goubault *et al.* (2003).

3.1. Linear dynamics of a filament perpendicular to the applied field

In the absence of a forcing time scale, we scale time by the elastoviscous time scale $T \equiv \alpha\zeta L^4/K_b$. For small deformations of the filament away from orthogonality to the field: $\theta \equiv \Theta + \pi/2$, we may linearize the system (2.15). It is seen that the tension vanishes along the length of the filament, and that (2.15b) and (2.17) reduce to

$$\frac{\partial\Theta}{\partial t} = -\frac{\partial^4\Theta}{\partial s^4} - M_n \frac{\partial^2\Theta}{\partial s^2}, \quad \frac{\partial\Theta}{\partial s} \Big|_{s=\pm 1} = \frac{\partial^2\Theta}{\partial s^2} + M_n\Theta \Big|_{s=\pm 1} = 0. \quad (3.1)$$

We solve this equation completely by seeking eigenfunctions of the associated linear operator:

$$\left(\mathcal{L}_1 \equiv \frac{\partial^4}{\partial s^4} + M_n \frac{\partial^2}{\partial s^2} \right) \hat{\Theta} = -\beta \hat{\Theta}. \quad (3.2)$$

Such eigenfunctions will evolve in time as $\Theta(s, t) = \hat{\Theta}(s; \beta)e^{\beta t}$. Eigenfunctions with multiple turning points, which we expect to be the linear precursors of the many-folded conformations observed by Goubault *et al.* (2003), have growth rates $0 < \beta < M_n^2/4$, and because of the symmetry of the operator \mathcal{L}_1 can be divided into even- and odd-parity solutions with respective forms

$$\hat{\Theta}_e(s; \beta) = A_\beta \cos k_\beta s + a_\beta \cos K_\beta s, \quad \hat{\Theta}_o(s; \beta) = B_\beta \sin k_\beta s + b_\beta \sin K_\beta s, \quad (3.3)$$

where

$$k_\beta^2 = \frac{1}{2}(M_n - \sqrt{M_n^2 - 4\beta}), \quad K_\beta^2 = \frac{1}{2}(M_n + \sqrt{M_n^2 - 4\beta}). \quad (3.4)$$

In order for the boundary conditions to be simultaneously realizable by some choice of the coefficients a_β and A_β or b_β and B_β then – according to the parity of the solution sought – it is necessary that β satisfy one of the equations

$$\text{even: } k_\beta^3 \tan k_\beta = K_\beta^3 \tan K_\beta \quad \text{or odd: } k_\beta^3 \cot k_\beta = K_\beta^3 \cot K_\beta. \quad (3.5)$$

As M_n is increased ‘higher-order’ unstable modes become available by an exchange of stabilities, so that an eigenmode with n arches exists if and only if

$$M_n \geq n^2\pi^2/4. \quad (3.6)$$

(The cases $n = 1$ and $n = 2$ require special treatment; see §3.2 below). An equivalent presentation of this criterion is in the form of a condition upon the length of the filament $L > nL_m$, for which we define a *magnetoelastic persistence length*:

$$L_m^2 \equiv \frac{3\pi\mu_0 K_b}{8a^2 B_c^2} \frac{(1 - \chi_{=}/6)(1 + \chi_{\perp}/12)}{\chi_{=} - \chi_{\perp} + \chi_{=}\chi_{\perp}/4}. \quad (3.7)$$

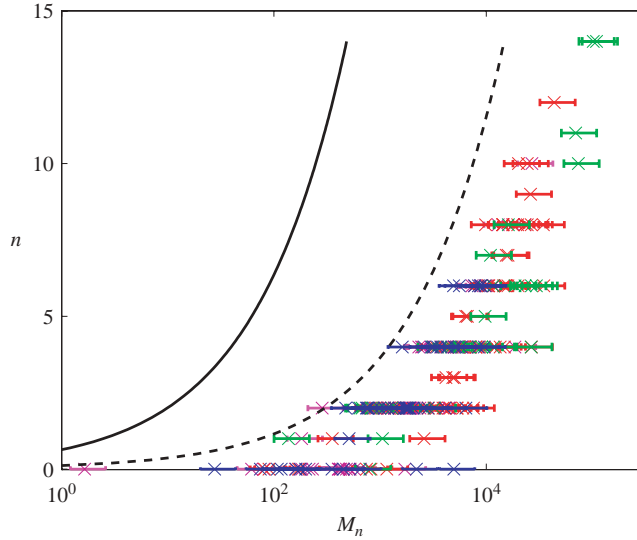


FIGURE 4. Test of linear dynamics as a predictor for the number of arches formed, n , as a function of the magnetoelastic number, M_n . The sequence of applied fields is described in the text and filaments of lengths ranging from $10\ \mu\text{m}$ up to $150\ \mu\text{m}$ are constructed from particles of diameter $2a = 750\ \text{nm}$ (Ademtech) linked by polyacrylic acid, with bending stiffness $K_b = (6.3 \pm 2.3) \times 10^{-24}\ \text{J m}$, and susceptibility $\chi = 1.62$. Different coloured data-sets correspond to different field strengths: $B_c = \sqrt{B_t^2 + B_o^2} = 6.21\ \text{mT}$ (magenta) $B_c = 8.97\ \text{mT}$ (blue); $B_c = 12.44\ \text{mT}$ (red) and $B_c = 17.80\ \text{mT}$ (green). The error bars reflect uncertainty in bending stiffness. The solid curve represents the lower bound derived in §3.1 based on linear dynamics, and the dashed curve the criterion ($M_n/n^2 > 75$) postulated in §3.2 on stability grounds.

The same result has also been derived by Cēbers (2005). Arguing that each multiply folded metastable configuration must form from a linearly unstable mode with the same or a greater number of folds, we posit that the criterion (3.6) will set the minimum length of a filament for it to form a metastable shape of n -folds. The results of a simple experimental assay to test this hypothesis are shown in figure 4. In the experiments (which follow the methodology of Goubault *et al.* 2003), filaments are first allowed to align with a weak magnetic field of strength $B_t = 1.4\ \text{mT}$, and then a much stronger orthogonal B_o field is quickly switched on. This procedure differs slightly from the scenario described in our linear stability analysis, by the presence of a small residual magnetic field component parallel to the filament. In the experimental assays, a large number of filaments are initially aligned with the weak field, a transverse field is applied, and the steady configurations attained by the filaments are then imaged. The number of folds in each of the steady configurations is then recorded along with the measured length of the filament, and thence the magnetoelastic number, and they are both plotted in figure 4. Data sets of different colours come from different assays, with the corresponding field strengths noted in the caption to the figure.

Evidently, the linear instability criterion (3.6) provides only a very slack lower bound upon M_n for arches to be observed. The mode structure seen at early times cannot alone determine the final configuration of the system. We indicate in §3.2 that a much stronger lower bound may come from the requirement that the static conformation be linearly stable. Two features of figure 2 are also in disagreement with

linear theory. Evolution toward the hairpin shape is seen at a magnetoelastic number $M_n = 0.1$, which is much less than the critical number $M_n = \pi^2/4$ for buckling given by (3.6). In fact the $n = 1$ mode must be treated separately from higher-order modes, as will be shown in §3.2. The simulated hairpin also develops an inflection point at its midpoint as it approaches a fully straightened state. No such inflection point is seen in the experimental time images. The difference cannot be attributed to the different parameters in the two plots; a near-straightened filament adopts the shape of the slowest decaying linear mode, which can be shown, by an analysis similar to that undertaken above, to always have an inflection point. It is likely that the discrepancy in this case originates from the relative weakness of the magnetic field, and the consequently greater role of heterogeneities in the filament bending stiffness, whose influence is discussed in §4.

3.2. Formation and stability of a simple hairpin

At moderate M_n exceeding the critical values identified in §3.1, the static hairpin is vulnerable to invasion by unstable modes, as shown in the numerical simulations presented in figure 3(b). Ensuring that the conformation is stable imposes much stiffer bounds upon M_n than the existence of buckling modes with the required number of arches. We will examine this for the case of a simple hairpin.

We begin by noting that the criterion for the existence of linear modes with n arches derived in §3.1 should not be applied to $n = 1, 2$, since it was arrived at by excluding modes with growth rates $\beta > M_n^2/4$, and address here the existence of more rapidly growing modes. The even- and odd-parity solutions have respective forms

$$\hat{\Theta}_e(s; \beta) = C_\beta \cosh ps \cos qs + c_\beta \sinh ps \sin qs, \quad (3.8a)$$

$$\hat{\Theta}_o(s; \beta) = D_\beta \cosh ps \sin qs + d_\beta \sinh ps \cos qs, \quad (3.8b)$$

where the exponents p, q are related to the coefficients of the differential equation by

$$(p + iq)^2 = \frac{1}{2}(-M_n + i\sqrt{4\beta - M_n^2}). \quad (3.9)$$

In order for the boundary conditions to be simultaneously realizable by some choice of C_β and c_β , or D_β and d_β , we must have respectively

$$\text{even: } q(M_n - p^2 - q^2) \sinh 2p = -p(M_n + p^2 + q^2) \sin 2q, \quad (3.10a)$$

$$\text{odd: } q(M_n - p^2 - q^2) \sinh 2p = p(M_n + p^2 + q^2) \sin 2q. \quad (3.10b)$$

One can show with a little algebra that the first equation has a single root provided that $\sin \sqrt{2M_n}/\sqrt{2M_n} \leq 1/3$, i.e. $M_n \geq 2.597$, while the second equation also has a single root, but that this exists for all positive M_n . Even eigenmodes have two arches, and odd eigenmodes a single arch; so it is tempting to identify these linear modes as the progenitors of the doubly and singly folded hairpins that were observed by Goubault *et al.* (2003).

It is useful in this vein to ask which of the eigenmodes is more unstable. Numerical solution of the pair of equations (3.10) shows that while the even mode is initially the most unstable, it is overtaken by the odd mode if the magnetoelastic number M_n is increased to a value $M_n^c = 3.290$. At higher values of M_n the two modes alternate as most unstable: see figure 5 in which the linear growth rate β is plotted as a function of M_n . The shapes of the even and odd perturbations are shown in figures 5(b) and 5(c). In the limit $M_n \gg 1$ one can show that the odd and even modes have respective

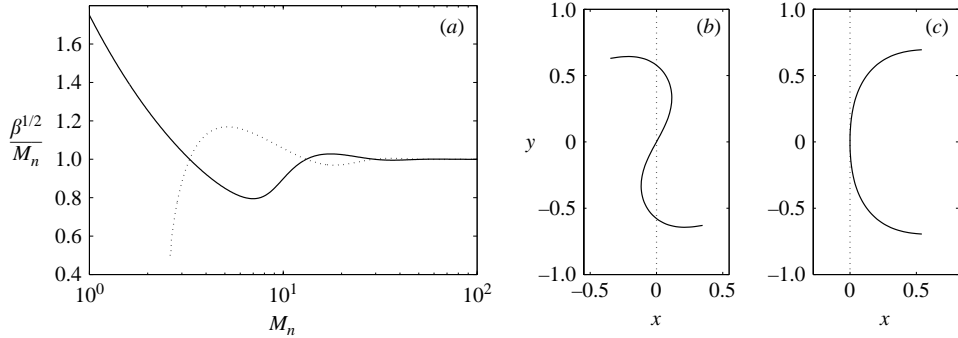


FIGURE 5. (a) Scaled growth rates of maximally unstable even- (solid line) and odd-parity (dotted line) modes. Corresponding mode shapes are shown (exaggerated) as (b, even) and (c, odd).

asymptotic growth rates

$$\beta = M_n^2 \left(1 \mp \frac{4}{\sqrt{3}} \frac{\sin \sqrt{3M_n}}{\sinh \sqrt{M_n}} \right) \quad (3.11)$$

so that to leading order, whether the most unstable mode has odd or even parity is controlled simply by the sign of $\sin \sqrt{3M_n}$. The exponential growth of the denominator in (3.11) makes this analytical criterion extremely accurate: its prediction that the first transition occurs at $M_n = \pi^2/3$ is indistinguishable to three decimal places from the numerically obtained value.

We now allow the two modes to evolve numerically using the fully nonlinear equations of motion and inextensibility (2.15). For sufficiently strong magnetic fields the odd mode evolves to a hairpin. We can calculate the final equilibrium shape exactly: the solution of the equilibrium equations compatible with the boundary conditions has

$$\Lambda \equiv 0, \quad N \equiv 0 \quad \text{or} \quad \frac{\partial^2 \theta}{\partial s^2} = \frac{M_n}{2} \sin 2\theta \quad (3.12)$$

(Goubault *et al.* 2003). If we introduce a scaled arclength $\bar{s} = M_n^{1/2}s$, and measure angles with respect to the field-orthogonal direction ($\theta = \pi/2 + \Theta$) then (3.12) reduces to the equation of a simple pendulum:

$$\frac{\partial^2 (2\Theta)}{\partial \bar{s}^2} = -\sin 2\Theta \quad \text{subject to} \quad \frac{\partial \Theta}{\partial \bar{s}} \Big|_{\bar{s}=\pm M_n^{1/2}} = 0. \quad (3.13)$$

Provided that $M_n > \pi^2/4$, (3.13) can be solved exactly in terms of Jacobi amplitudes: with angle and arclength variables related by an expression

$$\int_0^\Theta \frac{d\Theta'}{\sqrt{\cos 2\Theta' - \cos 2\Theta_0}} = -\frac{\bar{s}}{\sqrt{2}}, \quad (3.14)$$

where $\Theta_0 = \Theta(\bar{s} = -\sqrt{M_n})$ is given implicitly in terms of the magnetoelastic number by $K(\sin \Theta_0) = \sqrt{M_n}$ so that $\Theta_0 \sim \pi/2 - 4\sqrt{2}e^{-\sqrt{M_n}}$ as $M_n \rightarrow \infty$. Figure 6 shows the collapse of the filament shapes to a single universal form (corresponding to the solution of (3.13) with $\Theta_0 = \pi/2$) at large magnetoelastic numbers.

Perturbing around this analytical expression for the hairpin shape we can estimate the lifetime of the hairpin by a second stability analysis. Introducing perturbation

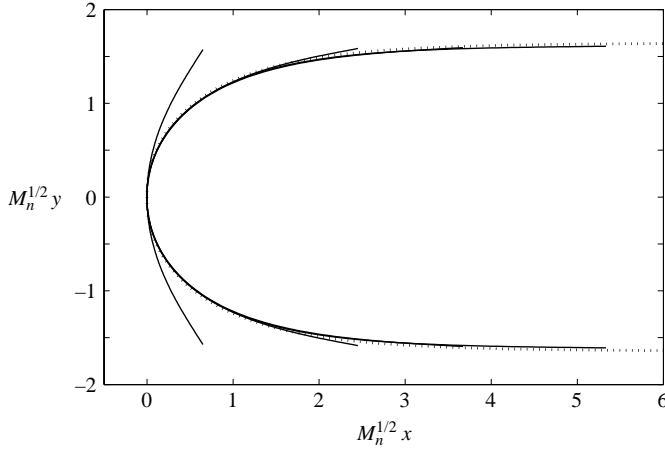


FIGURE 6. Universal form of the hairpin configurations. The x - and y -axes are scaled by $M_n^{1/2}$. Solid lines represent evolved solutions for $M_n=3.0, 10.1, 19.3, 36.7$; the dotted line is the $M_n \rightarrow \infty$ asymptote: $\log(\sec \Theta + \tan \Theta) = -\bar{s}$.

quantities $\Lambda \equiv M_n \Lambda'$, $\theta = \pi/2 + \Theta + \theta'$, and scaling time $\bar{t} = M_n^2 t$ and arclength $\bar{s} = M_n^{1/2} s$, we arrive at the linear instability equations

$$\alpha \frac{\partial^2 \Lambda'}{\partial \bar{s}^2} = \frac{\Lambda'}{2} (\cos 2\Theta - \cos 2\Theta_0) + \left(\frac{(\alpha + 1)}{\sqrt{2}} (\cos 2\Theta - \cos 2\Theta_0)^{1/2} \frac{\partial}{\partial \bar{s}} + \frac{\alpha}{2} \sin 2\Theta \right) \left(\frac{\partial^2 \theta'}{\partial \bar{s}^2} + \theta' \cos 2\Theta \right), \quad (3.15a)$$

$$\frac{\partial \theta'}{\partial \bar{t}} = -\frac{\Lambda'}{2} \sin 2\Theta - \frac{(\alpha + 1)}{\sqrt{2}} (\cos 2\Theta - \cos 2\Theta_0)^{1/2} \frac{\partial \Lambda}{\partial \bar{s}} + \left(\frac{\alpha}{2} (\cos 2\Theta - \cos 2\Theta_0) - \frac{\partial^2}{\partial \bar{s}^2} \right) \left(\frac{\partial^2 \theta'}{\partial \bar{s}^2} + \theta' \cos 2\Theta \right), \quad (3.15b)$$

subject to boundary conditions

$$\left(\frac{\partial^2 \theta'}{\partial \bar{s}^2} + \theta' \cos 2\Theta \right) \Big|_{\bar{s}=\pm\sqrt{M_n}} = \frac{\partial \theta'}{\partial \bar{s}} \Big|_{\bar{s}=\pm\sqrt{M_n}} = \Lambda' \Big|_{\bar{s}=\pm\sqrt{M_n}} = 0. \quad (3.16)$$

The filament is locally absolutely stable: localized disturbances are quickly annihilated by the bending stiffness, represented by the hyper-diffusive term. Since time does not appear explicitly in (3.15) it suffices to seek global modes: $\Lambda'(\bar{s}, \bar{t}) = \tilde{\Lambda}(\bar{s}) e^{\beta \bar{t}}$, $\theta'(\bar{s}, \bar{t}) = \tilde{\theta}(\bar{s}) e^{\beta \bar{t}}$ and solve numerically the corresponding linear generalized eigenvalue problem. The evolution with magnetoelastic number of the eigenvalues corresponding to the most unstable modes of the hairpin is shown in figure 7(a). In figure 7(b), the mode shapes of the unstable and slowest decaying stable modes are plotted. The single linearly unstable mode approaches, in the limit $M_n \rightarrow \infty$, neutral translation in \bar{s} of the basic profile: $\tilde{\theta} \propto \partial \Theta / \partial \bar{s}$. This perturbation function $\tilde{\theta}(s)$ is not admissible at any finite M_n since it disagrees by some $O(\exp \sqrt{M_n})$ amount with the boundary conditions (3.16). The scale of the correction that must be made to ensure compatibility with boundary conditions sets the growth rate of the most unstable mode, and so accounting for our rescaling of the time variable, we expect the filament to have an

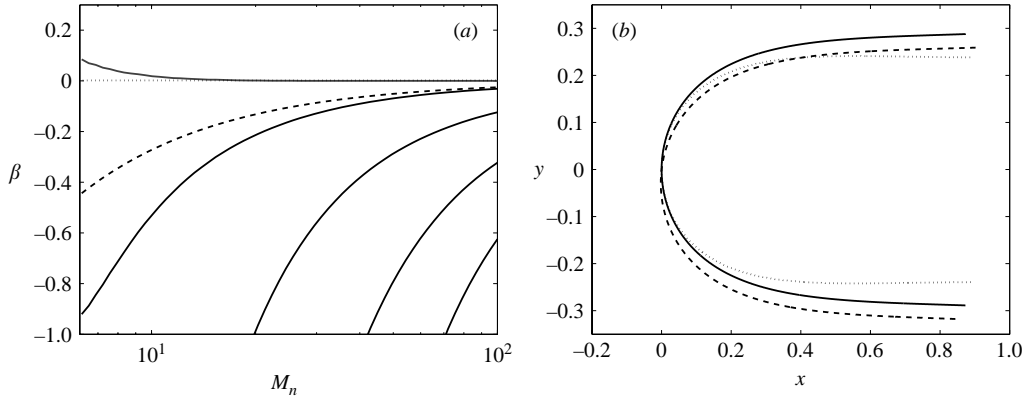


FIGURE 7. (a) Variation in growth rates of linear modes with M_n , for $\alpha=2.0$. Dotted line indicates marginal stability, and the dashed curve is the slowest relaxing mode of a straight filament of length L in near alignment with the magnetic field. (b) Linear mode shapes for $M_n=30$ $\alpha=2.0$, the solid curve is the equilibrium shape, the dashed curve is the maximum unstable mode, and the dotted curve the slowest decaying stable mode.

$O(M_n^{-2} \exp \sqrt{M_n})$ lifetime (measured in units of the elastoviscous relaxation time) in the limit of large magnetoelastic numbers. At moderate magnetoelastic numbers this lifetime may be extremely short: for instance at $M_n=10$, the exponential growth rate of this unstable mode is numerically determined to be $\beta=0.018$, giving it a lifetime of $T=1/M_n^2\beta \approx 0.5$. This is comparable to the time required for hairpin formation, and so we expect no hairpin shapes to be observed at or below this value of the magnetoelastic number.

The other modes of the filament are all stable down to arbitrarily small magnetoelastic numbers, and have lifetimes inversely proportional to M_n at large M_n . The rate at which each of these modes decays is controlled by the resistance arising from bending stress in the central arch of the hairpin. This point is made evident when the decay is contrasted with the much more rapid relaxation to complete alignment with a magnetic field of a filament of length L , representing one of the severed arms of the hairpin, which can be deduced from a linear stability analysis of the $\theta=0$ equilibrium state and is shown as the dashed curve in figure 7(b). In this case, deformations are eliminated at a rate asymptotically equal to $\beta \sim \pi^2 M_n$ (in units of the elastoviscous time).

We can use these results to revise the lower bound upon M_n for the formation of multiply folded structures that was derived in §3.1. Thus, even though the linear precursor to a simple hairpin exists down to $M_n=\pi^2/4$, such hairpins are only asymptotically stable in the limit of large magnetoelastic numbers. For a filament configuration to survive for the duration of the experiment, it is necessary that the exponential growth time $1/\beta$ greatly exceed the duration of the experiment. For the shortest hairpin observed in the series of experiments depicted in figure 4, $L=3.8\ \mu\text{m}$, so that for a hairpin to survive an experiment of duration T_e , we must have $\alpha\zeta L^4/\beta K_b > T_e$. The filament-perpendicular drag coefficient (which is greatly augmented by the proximity to the floor of the capillary tube) can be measured from assays of short filaments undergoing near rigid-body rotation under oscillatory magnetic fields (Dreyfus 2005); $\alpha\zeta \approx 1.3 \times 10^{-2}\ \text{Pa s}^{-1}$, and using the experimental values of K_b , χ and a (given in the caption to figure 4) we see that if $T_e=10\ \text{min}$ we must have $\beta < 4.1 \times 10^{-4}$, which is obtained for $M_n > 75 \pm 10$ (the precise

determination of this threshold is difficult at such small values of β), or to a field strength $B_c = 13$ mT. The series of assays recorded in figure 4 includes a hairpin of this length obtained at a field strength $B_c = 17.8$ mT, indicating that this is a physically reasonable condition. Moreover because our previous arguments give $\beta = O(M_n^2 \exp(-\sqrt{M_n}))$, the condition for survival of a hairpin over the duration of an experiment may be expressed as a critical condition upon M_n (i.e. upon the product $B_c L$) with only weak (logarithmic) direct dependence upon L through the ratio of time scales $T_e/(\alpha \zeta L^4/K_b)$. Extending the stability analysis given above to multiply folded filaments is difficult, since there is no analytical form for the base state, and direct simulation of the instability is hindered by the need to resolve extremely small radii of curvature at the folds. However, for a filament of n folds it is likely that the survival condition may be expressible as a critical bound upon an intensive magnetoelastic number $m_n \equiv M_n/n^2$ defined using the length of filament between arches $\ell = L/n$ instead of the full length. Using our survival criterion for the hairpin, we use the postulated condition $m_n > 75$ to compute a much tighter lower bound for the appearance of multiply folded filaments, shown as the dashed curve in figure 4.

Hairpins have also been shown to be stable under finite time-oscillatory transverse magnetic fields (Dreyfus 2005). Previously this anomalous stability has been attributed to magnetic heterogeneity (Cēbers 2005). However, after the magnetic field has been switched off the relaxed filaments often retain residual curvature typically of order $0.1 \mu\text{m}^{-1}$ for the PAA-bonded chains assayed in figure 4 (Dreyfus 2005), indicating that the severe strains associated with hairpin formation may induce irreversible (plastic) deformations of the polymer bridges between particles. This observation is also consistent with data presented in figure 3 of Goubault *et al.* (2003), in which hairpins of non-zero curvature are predicted by extrapolating the field strength to zero. Plastic deformation in the hairpin arch suffices to completely stabilize a filament, by eliminating the single unstable eigenmode, which we have seen corresponds, at large enough M_n , to translation of the filament along its length, and it is tempting to speculate that attaining curvatures large enough to induce plastic deformation may be a constraint for the realization of hairpin structures. However, there is no signature of this behaviour in figure 4, for in a simple model in which plastic deformation occurs only when the curvature at the midpoint of the arch exceeds some critical value κ_c (say), our condition for deformation may equivalently be written in terms of the transformed coordinates introduced above as $\partial\Theta/\partial\bar{s}(s=0) \approx 1/2 > \kappa_c L/M_n^{1/2}$, which, apart from logarithmic corrections, gives us a bound that features the field strength only, and does not depend upon the length of the filament. Thus two filaments of different lengths should have equal capacity to form hairpins under the same magnetic field, contrary to the trend shown in figure 4.

4. Defect-provoked swimming

It is observed experimentally that even if both ends of a magnetic filament are left free, it may be capable of swimming under the combination of fields (uniform in the direction of motion with a sinusoidally varying orthogonal component) identified above. For the fore-aft symmetry to be broken, one of our assumptions about the homogeneity of the magnetic and elastic properties must be violated. Since the number of polymer linkages between the particles in the filament is difficult to control experimentally, we expect some variation in bending stiffness along the length of the filament. In fact, close examination of time-series images of swimming filaments shows that, without exception, each has a visible defect: at least one obviously malformed

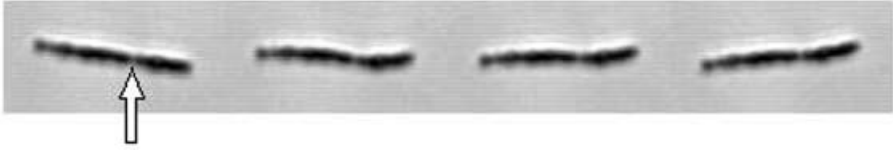


FIGURE 8. Images of a swimming filament. Experimental parameters: length $2L = 20 \mu\text{m}$, field strengths $B_c = 50 \text{ mT}$ and $B_0 = 70 \text{ mT}$, $\omega = 100\pi \text{ s}^{-1}$, swimming speed $\langle v_x \rangle \approx 2 \mu\text{m s}^{-1}$ to the right. The arrow indicates location of the apparent defect.

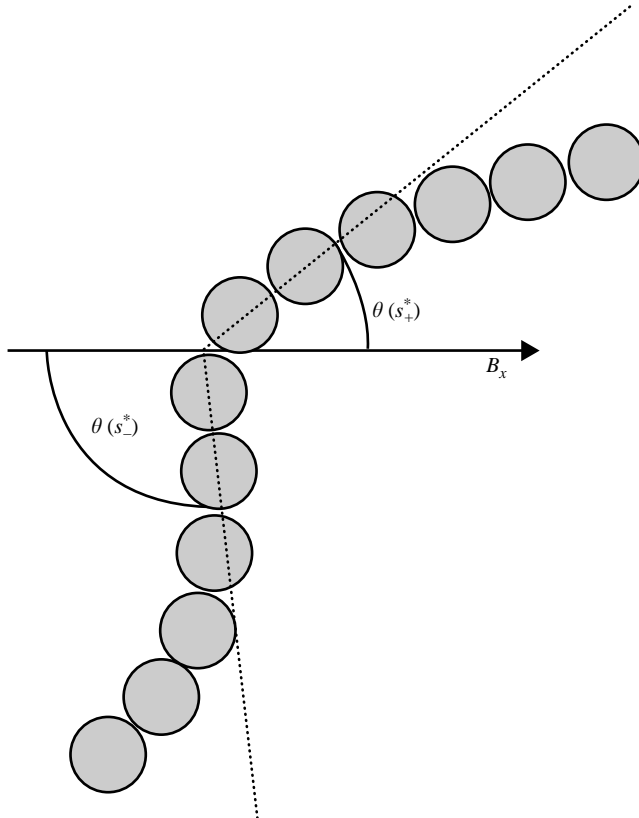


FIGURE 9. Schematic of a filament with a single defect at a site $s = s^*$. We denote by $s = s_-^*$ and $s = s_+^*$ material points just to the left and to the right of the defect.

contact between some pair of particles. A typical series of images illustrating such a defect is given as figure 8. While it is more likely that symmetry is broken by a variation in bending stiffness along the filament, here we investigate how much useful physics can be extracted from a simple mode of elastic symmetry breaking: the inclusion of a single defect.

We model the defect by imagining that the polymer bridge between one pair of particles in the filament, though able to maintain their adjacency, has no inherent bending stiffness and cannot transmit torques. In our continuum model for the filament this means permitting a step discontinuity in the angle θ at some value of the arclength parameter $s = s^*$; see figure 9. No torque can be exerted upon this linker,

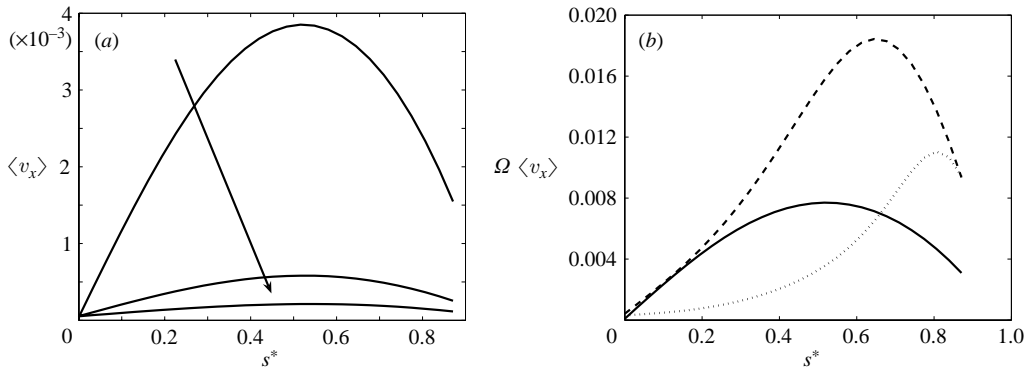


FIGURE 10. Swimming velocity as a function of defect location (s^*), showing variation with (a) magnetoelastic number M_n , at constant $\Omega = 2.0$ and (b) frequency at constant $M_n = 1.0$. In (a) arrow denotes increasing M_n , for values $M_n = 1.0, 5.0, 10.0$. In (b) the solid line represents $\Omega = 2.0$, the dashed line $\Omega = 20.0$, and the dotted line $\Omega = 80.0$. In (b) we plot the scaled velocity $\Omega \langle v_x \rangle$ (distance travelled per unit time, rather than per stroke) to eliminate spurious frequency dependence. All data sets are obtained with $b_0 = 0.5$, $\alpha = 2.0$ and $N_p = 81$.

so that we must have vanishing bending moment as the defect is approached from either side: $\partial\theta/\partial s|_{s=s_{\pm}^*} = 0$.

Additionally, balances of tangential and normal forces acting on the linker give respective conditions

$$[\Lambda \cos \theta - N \sin \theta]_{s=s_{-}^*}^{s=s_{+}^*} = [\Lambda \sin \theta + N \cos \theta]_{s=s_{-}^*}^{s=s_{+}^*} = 0. \quad (4.1)$$

Assuming that the length of the linker (and thus the relative motion of the two ends of the filament $s = s_{\pm}^*$) can be neglected, we may equate the velocities of the two ends and arrive at an additional pair of boundary conditions:

$$[v_s \cos \theta - v_n \sin \theta]_{s=s_{-}^*}^{s=s_{+}^*} = [v_s \sin \theta + v_n \cos \theta]_{s=s_{-}^*}^{s=s_{+}^*} = 0. \quad (4.2)$$

Applying these six conditions on the angle and tension variables at the defect we can solve the governing PDEs numerically.

4.1. Kinematics of swimming: moderate frequencies

Having broken free from fore–aft symmetry, the filament is now able to swim, but just as with Purcell’s three-link swimmer, there is no *a priori* way of determining in which direction it swims. We let s^* range from -1 to 1 , give the filament enough time to forget its starting configuration and attain a periodic swimming state, and determine its period-averaged swimming velocity. In figure 10 we demonstrate the effect upon the swimming velocity of varying the location of the defect s^* , the magnetoelastic number M_n , and the frequency of the transverse field Ω . For small to moderate values of the transverse field strength b_0 , the filament always swims towards the defect (i.e. to the left if $s^* < 0$ and to the right if $s^* > 0$). In order to explain the phenomenology of the swimming stroke, we illustrate with figures 11(a), and 12(a,b) typical conformations adopted by the filament, while for comparison figure 11(b) shows the affect of applying the same configuration of fields to a filament with no elastic defects.

The set of conformations for a high-frequency swimmer (figure 12a, b) resemble a variant of the three-link swimmer proposed by Purcell (1977), and analysed completely by Becker *et al.* (2003). The same ideas of passive and active elements developed in

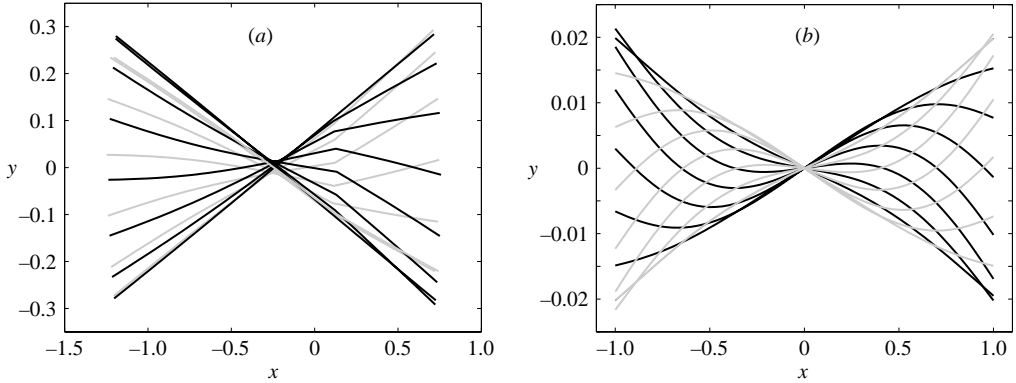


FIGURE 11. (a) Kinematics of the swimming stroke at low ($M_n = 1.0, \Omega = 2.0$) frequency. The defect is located at $s^* = 0.32$. (b) Stroke of filament at $\Omega = 80$ without defect for contrast with figure 12(a, b). As a visual aid, the cycle is split into two halves: defect point moving in the negative y -direction (black curves), and defect point moving in the positive y -direction (grey curves) Both simulations are performed with $b_0 = 0.5$ and $N_p = 81$.

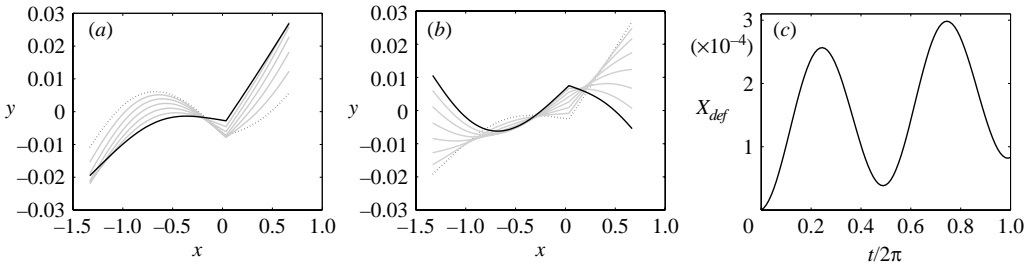


FIGURE 12. (a) Thrust, (b) recovery. $M_n = 1.0, \Omega = 80, b_0 = 0.5$ and $N_p = 81$. The transverse field $b_0 \sin t$ decreases from b_0 to $-b_0$ over the half-cycle. The dotted line represents the initial shape, the solid line the final shape, and grey lines intermediate shapes. The remaining half of the cycle can be obtained by mirror reflection in the x -axis. (c) x -displacement of the defect during the stroke sequence.

that paper can be applied to this swimmer, albeit with caution since both extremities are active at the same time, and torques are generated along the filament rather than exclusively at joints. To describe the stroke pattern of the filament at high frequencies, we split the stroke into two parts: ‘thrust’ and ‘recovery’. Consider the force generated at the rightward end of the longer arm of the filament – in the ‘thrust’ phase the angle made by the arm at the defect is decreasing, and net force acts in the positive x -direction (analogous to the motion achieved by Purcell’s hypothetical low-Reynolds-number scallop by shutting its shell). During ‘recovery’ the angle increases, and net force acts in the negative x -direction (scallop opening). The normal force at s^* is in general non-zero; it must be equated to the total viscous drag on the short (‘rudder’) arm of the filament, which suffices to break the fore–aft symmetry of the driving arm.

During the thrust phase the short arm relaxes out any curvature developed in the previous recovery stroke, and moves in the y -direction without any change of orientation. The total magnetic torque on the rudder, which is directed anticlockwise in figure 12(a), must be balanced by the normal stress moment (s -integrated normal stress) since there is no torque resultant at either end of the rudder. During ‘recovery’

(with the torque now directed clockwise) the rudder starts to rotate and to flex in the opposite sense. This means that the total torque, and by implication the normal force at the left-hand end, is reduced compared to the thrust stroke. Note that there is little translation of the centre of the rudder in figure 12(b) and that the driving arm deforms in a much more fore–aft-symmetric fashion. Displacement in the negative x -direction is less in recovery than that in the positive direction during thrust.

To make a quantitative study of the effect of varying the frequency, site of the defect, or magnetoelastic number upon the swimming speed of the filament, we examine the two analytically tractable limits in which the period of the transverse field is much longer or shorter than the elastoviscous time scale on which the filament is able to eliminate bending.

In the high-frequency limit ($\Omega \gg 1$, $\Omega \gg M_n$) it can be shown that deformation of the filament under the applied torques is confined to regions of length $O(\Omega^{-1/4})$ near the free ends; outside these bending boundary layers the filament remains aligned with the steady component of the applied magnetic field. The deformation is not severe and the evolution of the angle variable θ is governed by the hyper-diffusive equation studied by Wiggins & Goldstein (1998), with the magnetic torque not participating directly but featuring in the boundary conditions at $s = s^*$ and $s = 1$. At large Ω defect-provoked swimming is only possible if s^* lies within one of the two bending boundary layers, the signature of which can be seen in the shift in the peak swimming speed toward $s^* = 1$ in figure 10(b).

4.2. Slowly varying magnetic field $\Omega \ll 1$

For a slowly varying transverse field, the filament tracks the local field direction almost as a rigid body. Kinematic reversibility makes this mode of swimming ineffective: whatever thrust is generated on one stroke is entirely repaid on the counter-stroke and any tendency to swim must come from the small flexure that develops at finite Ω . We pursue an expansion in powers of Ω of each of the system variables around the rigidly pivoting solution:

$$\theta(s, t) = \underbrace{\tan^{-1}(b_0 \sin t)}_{\theta_0(t)} + \Omega \theta_1(s, t) + \Omega^2 \theta_2(s, t) + \cdots, \quad \Lambda(s, t) = \Omega^2 \Lambda_2(s, t) + \cdots, \quad (4.3)$$

$$N(s, t) = \Omega N_1(s, t) + \Omega^2 N_2(s, t) + \cdots. \quad (4.4)$$

Note that the magnetic torque defined in §2.2 then becomes

$$M_n S(\theta, t) = M_n \Omega \theta_1(\partial S / \partial \theta)(\theta_0(t), t; b_0) + O(\Omega^2) = -\Omega \sigma^2 \theta_1 + O(\Omega^2), \quad (4.5)$$

where in order to simplify algebra in what follows we have defined a dimensionless local wavenumber, $\sigma(t; b_0) \equiv \sqrt{M_n(1 + b_0^2 \sin^2 t)}$. Substitution of this solution form into the equations of motion (2.15) and the expression for the normal stress resultant (2.10) yields at each order an uncoupled pair of differential equations.

At $O(\Omega)$ we seek solutions to

$$\frac{\partial \theta_0}{\partial t} = \frac{\partial^2 N_1}{\partial s^2}, \quad (4.6)$$

subject to a vanishing of normal stress $N_1 = 0$ at the free ends ($s = \pm 1$) while the continuity relations (4.1), (4.2) require that both N_1 and $\partial N_1 / \partial s$ vary continuously

over the defect $s = s^*$. The equation may be simply integrated up to obtain

$$N_1(s, t) = \frac{b_0 \cos t}{2(1 + b_0^2 \sin^2 t)}(s^2 - 1). \tag{4.7}$$

Now using the relation between θ_1 and N_1

$$-\frac{\partial^2 \theta_1}{\partial s^2} + \sigma^2 \theta_1 \equiv N_1 \tag{4.8}$$

together with the torque-free boundary condition at the free end $\partial \theta_1 / \partial s = 0$ at $s = \pm 1$ and at the defect $s = s^*$, we arrive at expressions

$$\theta_1^+(s, t) = \frac{M_n b_0 \cos t}{\sigma^4} \left[\frac{1}{2}(s^2 - 1) + \frac{1}{\sigma^2} + \frac{s^* \cosh(\sigma(s - 1)) - \cosh(\sigma(s - s^*))}{\sigma \sinh(\sigma(1 - s^*))} \right], \tag{4.9a}$$

$$\theta_1^-(s, t) = \frac{M_n b_0 \cos t}{\sigma^4} \left[\frac{1}{2}(s^2 - 1) + \frac{1}{\sigma^2} - \frac{s^* \cosh(\sigma(1 + s)) + \cosh(\sigma(s - s^*))}{\sigma \sinh(\sigma(1 + s^*))} \right], \tag{4.9b}$$

valid in the respective domains $s > s^*$ and $s < s^*$. The filament flexes and opens at the defect by an angle

$$\Delta \theta_1(t) \equiv \frac{\Omega M_n b_0 \cos t}{\sigma^5} [s^* \coth(\sigma(1 - s^*)) + s^* \coth(\sigma(1 + s^*)) - \operatorname{cosech}(\sigma(1 - s^*)) + \operatorname{cosech}(\sigma(1 + s^*))]. \tag{4.10}$$

At $O(\Omega^2)$ the continuity relations (4.1), (4.2) yield

$$[N_2]_{-}^{+} = \left[\frac{\partial N_2}{\partial s} \right]_{-}^{+} = 0, \quad [A_2]_{-}^{+} = N_1 [\theta_1]_{-}^{+}, \quad \left[\frac{\partial \Lambda}{\partial s} \right] = \frac{1}{\alpha} \frac{\partial N_1}{\partial s} [\theta_1]_{-}^{+}, \tag{4.11}$$

where we have used $[]_{-}^{+}$ as a shorthand for denoting the discontinuity in a variable across $s = s^*$. We can therefore solve separately for Λ_2 and N_2 . We simplify the algebra by solving for the time-integrated normal stress, $\mathcal{N}_2 \equiv \int^t N_2 dt$, which satisfies equations

$$\frac{\partial^2 \mathcal{N}_2^{\pm}}{\partial s^2} = \theta_1^{\pm} \quad \text{with} \quad \mathcal{N}_2^{\pm}|_{s=\pm 1} = 0, \quad [\mathcal{N}_2]_{-}^{+} = \left[\frac{\partial \mathcal{N}_2}{\partial s} \right]_{-}^{+} = 0, \tag{4.12}$$

from whence we obtain expressions

$$\mathcal{N}_2^+ = \frac{M_n b_0 \cos t}{\sigma^4} \left[\frac{1}{24}(s^4 - 6s^2 + 5) + \frac{s^2 - 1}{2\sigma^2} + C(s - 1) + \frac{s^* \cosh(\sigma(s - 1)) - s^* - \cosh(\sigma(s - s^*)) + \cosh(\sigma(1 - s^*))}{\sigma^3 \sinh(\sigma(1 - s^*))} \right], \tag{4.13}$$

$$\mathcal{N}_2^- = \frac{M_n b_0 \cos t}{\sigma^4} \left[\frac{1}{24}(s^4 - 6s^2 + 5) + \frac{s^2 - 1}{2\sigma^2} + C(s + 1) - \frac{s^* \cosh(\sigma(s + 1)) - s^* + \cosh(\sigma(s - s^*)) + \cosh(\sigma(1 + s^*))}{\sigma^3 \sinh(\sigma(1 + s^*))} \right], \tag{4.14}$$

where the coefficient C is chosen to satisfy the continuity relations

$$C = \frac{s^* \sinh \sigma - \sinh(\sigma s^*)}{\sigma^3 (\cosh(\sigma s^*) + \cosh \sigma)}. \tag{4.15}$$

At the same time, it is necessary to solve for the second-order tension contribution from the inextensibility equation

$$\alpha \frac{\partial^2 \Lambda_2^\pm}{\partial s^2} = (\alpha + 1) \frac{\partial \theta_1^\pm}{\partial s} \frac{\partial N_1}{\partial s} + \alpha \frac{\partial^2 \theta_1^\pm}{\partial s^2} N_1. \quad (4.16)$$

A closed-form expression for the tension is long and we do not reproduce it here.

The time-integrated swimming speed of the filament is given correct to leading order in Ω by the expression

$$\langle v_x \rangle = \frac{\Omega}{2\pi} \int_0^{2\pi} \left(\left(\frac{\partial \Lambda_2}{\partial s} - \theta_1 \frac{\partial N_1}{\partial s} \right) \cos \theta_0 - N_2 \sin \theta_0 \right) \Big|_{s=s^*} dt \quad (4.17a)$$

$$= \frac{\Omega}{2\pi} \int_0^{2\pi} \left(\left(\frac{\partial \Lambda_2}{\partial s} - \theta_1 \frac{\partial N_1}{\partial s} \right) \frac{1}{(1 + b_0^2 \sin^2 t)^{1/2}} + \mathcal{N}_2 \frac{b_0 \cos t}{(1 + b_0^2 \sin^2 t)^{3/2}} \right) \Big|_{s=s^*} dt, \quad (4.17b)$$

where we have recast the integral in terms of the time-integrated normal stress \mathcal{N}_2 by integrating by parts. The expression for the swimming speed includes contributions from tension and a time-non-reversible normal force. That the velocity is $O(\Omega)$ at sufficiently small Ω could have been anticipated from a simple symmetry argument: setting $\Omega \rightarrow -\Omega$ is equivalent to reversing the direction of the y -coordinate axis and reversing the direction of time, so that we then expect $\langle v_x \rangle \rightarrow -\langle v_x \rangle$, and that velocity must be at least $O(\Omega)$ in this parameter range. The dimensional velocity will therefore be proportional to the square of the dimensional frequency. In general the integral in (4.17b) must be evaluated numerically; however, much of the phenomenology of swimming can be understood by the consideration of two distinguished limits.

4.2.1. $M_n \rightarrow 0$

As the magnetoelastic number $M_n \rightarrow 0$, corresponding to a short stiff filament or to a weak magnetic field, the leading-order swimming speed of the filament is

$$\langle v_x \rangle \sim \frac{\Omega(\alpha - 1)}{24M_n\pi} s^*(1 - s^{*2}) \int_0^{2\pi} \frac{b_0^2 \cos^2 t dt}{(1 + b_0^2 \sin^2 t)^{7/2}} + O(1), \quad (4.18)$$

which clearly displays the influence of the defect location. There is no translation if the defect is coincident with the midpoint, in which case fore–aft symmetry remains unbroken, or with either of the free ends of the filament, since then the ruddering mechanism described above cannot be employed. The maximum swimming speed is attained when $s^* = \pm 1/\sqrt{3}$ for rightward/leftward swimming.

Note that we seem to show here that the swimming speed of the filament becomes singular as we let $M_n \rightarrow 0$; in fact the low-frequency limit requires us to invoke the additional regularity assumption that $\Omega \ll M_n$. As $M_n \rightarrow 0$ the domain of validity of our asymptotic expressions becomes vanishingly small; however, holding Ω/M_n constant so as to maintain the compatibility of expansions, we conclude that the distance travelled by the filament per stroke remains finite in the limit of arbitrarily weak fields.

4.2.2. $M_n \rightarrow \infty$

For large M_n , i.e. a long flexible filament or strong magnetic field, it can be shown with some lengthy algebra that the time-averaged velocity decays with M_n like

$$\langle v_x \rangle = \frac{\Omega(\alpha - 1)s^*}{2\pi M_n^{5/2}} \int_0^{2\pi} \frac{b_0^2 \cos^2 t \, dt}{(1 + b_0^2 \sin^2 t)^5} + O(\exp[-M_n^{1/2}(1 - |s^*|)]). \quad (4.19)$$

In this strong field limit, the filament swims fastest if the defect is located near one of the free ends, though not within bending zones of length $O(M_n^{-1/2})$ at each end. Reducing the length of the ‘rudder’ improves its function, right down to a length at which it is no longer able to flex to accommodate the force difference between its two ends. One interpretation for this is that – just as in the picture of the stroke kinematics introduced above – the rudder is essentially passive, and reducing its length reduces the passive drag that resists the driving arm. Only when the length scale of the rudder becomes comparable with the thickness of the bending zone is information about the free end $s = 1$ communicated to the driving arm, so that the stroke becomes fore–aft symmetric, leading to a fall-off in swimming speed.

In both limits of M_n , we observe that if the perpendicular and parallel drag coefficients are identical (i.e. $\alpha = 1$) there is no net translation, illustrating the general result that drag-based swimming is impossible under conditions of isotropic drag (Becker *et al.* 2003). In both regimes the swimming speed decreases with M_n , which is also seen at moderate frequencies in our numerical results (figure 10); somewhat remarkably, depending on the location of the defect, stiff filaments can be more effective swimmers at low frequencies. For the filament shown in figure 8 $M_n = 16.3$ and we estimate (using the directly measured value of $\alpha\zeta = 1.3 \times 10^{-2} \text{ Pa s}^{-1}$) that $\Omega = 100$. Putting these parameters into the simulations (and putting an idealized defect at $s^* = 0.33$) gives $\langle v_x \rangle \approx 0.4 \mu\text{m s}^{-1}$, which is slightly smaller than the experimental value but certainly of the right order of magnitude.

4.3. *Strong transverse fields and hairpin stabilization*

Becker *et al.* (2003) find that Purcell’s three-link swimmer is biphasic: with the same stroke pattern the direction that the swimmer takes is reversed as the stroke amplitude is increased above a threshold that depends on the dimensions of the swimmer. This feature can be identified with the existence of a second mode of swimming for the swimmer, in which with two links together function as the rudder, with only one extremal link driving the system. It is natural to ask whether the same might be true of these paramagnetic swimmers. We have been able to find no evidence for this within experimentally realizable ranges of b_0 , M_n and Ω . It is possible for sufficiently small values of M_n and Ω and large b_0 and appropriately contrived initial configurations to obtain large discontinuities in angle $\theta(s_+^*) - \theta(s_-^*)$, but if this discontinuity exceeds $\pi/2$ (an approximate criterion for accessing the second swimming mode for the three-link swimmer) it suffers a ‘snap-through’ instability, where $|\theta(s_+^*) - \theta(s_-^*)| \rightarrow \pi$. Neither our hydrodynamic model, nor our expression for the torque can be applied to the doubled-back swimmer, nor is there any evidence of ‘snap-through’ in experiments. However, it is interesting to observe the effect of such transitions on the stability and range of static shapes available in experiment.

In static hairpins the magnetic torque is completely balanced by bending stiffness (Goubault *et al.* 2003), and no force acts normal to the filament. For this reason, a zero-bending-stiffness defect such as that under study is lethal if it occurs in the arch of a potential hairpin, since it permits the hairpin to fold completely shut without

any tensile or bending penalty. However, numerical simulations show that it is benign if included in one of the arms of the filament.

4.4. More general classes of defects

Our defect model is by design simple, and unlikely to correspond in detail to any of the range of defects encountered in experiment. However, it serves as a powerful proof of the principle that localized defects can account for at least part of the phenomenology of swimming in otherwise homogeneous filaments. Even without admitting the full richness of continuous variation in bending stiffness along the spine of the filament, one can conceive many other simple extensions to the theory, representing plausible forms of defect: a site of high bending stiffness (corresponding to increased polymer density), or localized natural curvature (a kink in the filament, as might occur if one of the beads slips out of alignment during the assembly phase).

5. Conclusions

We have applied slender-body theory to study the magnetically driven changes in conformation of a long filament consisting of linked paramagnetic particles. With this model, we have analysed the stability of a class of the static shapes available to the filament, with focus on the lifetime of a simple hairpin (Goubault *et al.* 2003). We have argued that such stability thresholds will provide the most accurate criteria for the observation of folded filaments in experiments.

We have also investigated the dynamical evolution of filaments under crossed steady and temporally varying magnetic fields with directed swimming triggered by the inclusion of elastic defects in the filament. The stroke was kinematically decomposed and numerical results for the swimming speed as a function of defect location and of the frequency and magnetoelastic number were computed. It would be interesting to extend this study to filaments with multiple defects. Comparison to experiment may become possible if a scheme for reproducibly manufacturing defects is devised.

While our model captures some of the rich dynamics of experiments, and provides robust scaling laws for the swimming speed as a function of frequency and magnetoelastic number, quantitative comparison with the experimental data will require further insight into the physics of the thin fluid layer separating the filament from the floor of the capillary tube.

The unprecedented control that Dreyfus *et al.* (2005) were able to exert over properties such as the length of the filament, time variation in the external field and rheology of the surrounding fluid makes this a very good system for testing our best understanding of swimming at low Reynolds number. Moreover, a quantitatively accurate theory for the swimming speed of such filaments might have practical utility. The swimming speed of the filament is controlled by its bending stiffness and this in turn is set by the number and quality of polymer links between the paramagnetic particles (Goubault *et al.* 2003). If the inverse function for obtaining the bending stiffness from the swimming speed can be found, then we are presented with the prospect of extracting information about the strength and affinity of the chemical contacts between polymer and particle coating from mesoscopic measurements of swimming speed without any direct manipulation of the particles in the filament.

The authors thank C. Goubault and P. Jop for inspiring this study, and for their help with materials preparation. M.R. and H.A.S. thank the Harvard NSEC and the benefactor of the Kao Fellowship for financial support.

REFERENCES

- AVRON, J. E., KENNETH, O. & OAKNIN, D. H. 2005 Pushmepullyou: An efficient micro-swimmer? *New J. Phys.* **7**, 234.
- BATCHELOR, G. K. 1970 Slender-body theory for particle of arbitrary cross-section in Stokes flow. *J. Fluid Mech.* **44**, 419–440.
- BECKER, L. E., KOEHLER, S. A. & STONE, H. A. 2003 On self-propulsion of micro-machines at low Reynolds number: Purcell's three-link swimmer. *J. Fluid Mech.* **490**, 15–35.
- BRENNEN, C. & WINET, H. 1977 Fluid mechanics of propulsion by cilia and flagella. *Annu. Rev. Fluid Mech.* **9**, 339–398.
- CAMALET, S., JÜLICHER, F. & PROST, J. 1999 Self-organized beating and swimming of internally driven filaments. *Phys. Rev. Lett.* **82**, 1590–1593.
- CĒBERS, A. 2005 Flexible magnetic swimmer. *Magnetohydrodynamics* **41**, 63–72.
- CĒBERS, A. & JAVAITIS, I. 2004 Buckling of flexible magnetic rods. *Phys. Rev. E* **70**, 021404.
- DREYFUS, R. 2005 Filaments magnétiques : application à la conception de capteurs de forces et de nageurs microscopiques artificiels. PhD thesis, ESPCI, Paris.
- DREYFUS, R., BAUDRY, J., ROPER, M. L., FERMIGIER, M., STONE, H. A. & BIBETTE, J. 2005 Microscopic artificial swimmers. *Nature* **436**, 862–865.
- GOUBAULT, C., JOP, P., FERMIGIER, M., BAUDRY, J., BERTRAND, E. & BIBETTE, J. 2003 Flexible magnetic filaments as micromechanical sensors. *Phys. Rev. Lett.* **91**, 260802.
- KOENIG, A., HÉBRAUD, P., GOSSE, C., DREYFUS, R., BAUDRY, J., BERTRAND, E. & BIBETTE, J. 2005 Magnetic force probe for nanoscale biomolecules. *Phys. Rev. Lett.* **95**, 128301.
- LAGOMARSINO, M., CAPUANI, F. & LOWE, C. 2003 A simulation study of the dynamics of a driven filament in an Aristotelian fluid. *J. Theor. Biol.* **224**, 215–224.
- MARTIN, J. E. & ANDERSEN, R. A. 1996 Chain model of electrorheology. *J. Chem. Phys.* **104**, 4814–4827.
- NAJAFI, A. & GOLESTANIAN, R. 2004 Simple swimmer at low Reynolds number: Three linked spheres. *Phys. Rev. E* **69**, 062901.
- PURCELL, E. M. 1977 Life at low Reynolds number. *Am. J. Phys.* **45**, 3–11.
- STRICK, T. R., ALLEMAND, J., BENSIMON, D., BENSIMON, A. & CROQUETTE, V. 1996 The elasticity of a single supercoiled DNA molecule. *Science* **271**, 1835–1837.
- VANDENBERGHE, N., ZHANG, J. & CHILDRESS, S. 2004 Symmetry breaking leads to forward flapping flight. *J. Fluid Mech.* **506**, 147–155.
- WIGGINS, C. H. & GOLDSTEIN, R. E. 1998 Flexive and propulsive dynamics of elastica at low Reynolds number. *Phys. Rev. Lett.* **80**, 3879–3882.
- WIGGINS, C. H., RIVELINE, D., OTT, A. & GOLDSTEIN, R. E. 1998 Trapping and wiggling: Elastohydrodynamics of driven microfilaments. *Biophys. J.* **74**, 1043–1060.
- ZHANG, H. & WIDOM, M. 1995 Field-induced forces in colloidal particle chains. *Phys. Rev. E* **51**, 2099–2103.